Terahertz Nondestructive Characterization of Conformal Coatings for Microelectronics Packaging

Haolian Shi, Serena Calvelli, Min Zhai, Marco Ricci, Stefano Laureti, P. Singh, H. Fu, Alexandre Locquet, D. Citrin

Terahertz Nondestructive Characterization of Conformal Coatings for Microelectronics Packaging

H. Shi, S. Calvelli, M. Zhai, M. Ricci, S. Laureti, P. Singh, H. Fu, A. Locquet and D.S. Citrin

***Abstract*—Measuring the thickness of conformal coatings and detecting defects in a nondestructive and noncontact fashion is important to ensure the reliability and performance of packaged electronic components and systems. In this study, we explore the application of terahertz time-of-flight tomography, a noncontact and nondestructive method here applied to conformal-coating thickness. We measure the time delay of terahertz pulses reflected (echoes) from fabricated structures covered by a conformal coating to ascertain its thickness. Orthogonal matching pursuit, is applied to deconvolve reflected terahertz signals from different interfaces, *viz.* air/conformal coating and conformal coating/substrate. By these means, we map the conformal-coating thickness distribution over significant areas. The conformal coating thickness found over the metal area is ∼64.3 µm while it is ∼56.2 µm over the metal-free area. Moreover, the Gaussian mixture model, a machine-learning algorithm, is used to detect a possible defect-rich region within the conformal coating itself.**

***Index Terms*—Conformal coating, THz-TDs, Gaussian mixture model, heterogeneous packaging, machine learning, nondestructive evaluating, nondestructive testing, orthogonal matching pursuit**

I. Introduction

To protect devices and systems mounted on printed circuit boards (PCB) from ambient gasses and water vapor that can attack microelectronics, a thin layer of synthetic resin or plastic is typically applied on top of packaged circuits [1], [2]. This thin layer of protection is called a conformal coating (CC). Typical CC materials include silicone, urethane, and acrylics [2]. Choice of CC material involves a balance of cost, degree of conformance, conditions under which the packaged circuit will operate, and the ability to make repairs on the CC.

In addition, although CCs are used to protect PCBs and mounted ICs and structures from harsh environments that can damage circuits, defects in manufacturing or failure in service in the CC itself may occur. Some common defects include capillary flow, cracking, dewetting, delamination, orange peel, and bubbles [3], [4]. Detecting these defects, especially in early stages, can help prevent future failure and assist in optimizing the CC deposition process. It can also save costs if they are detected during production. To evaluate the protection and performance of CCs, surface insulation resistance (SIR) and sequential electrochemical reduction analysis (SERA) are commonly used [5]. These techniques provide general information about the protection ability of the CC, but they may not be able to pinpoint where defects may lie. To locate the defect, visual inspection of the CC is often used [6]. However, such an approach is laborious and defects or degradation may escape visual detection.

In addition to defect detection, understanding the thickness of CC deposited is important to guarantee proper coverage, while excessive CC material may stress or otherwise compromise underlying circuitry. Excessive buildup of material might also be difficult to remove in making repairs. Methods to measure CC thickness include both destructive and nondestructive techniques. For destructive methods, most straightforward is cutting samples and measuring the cross-section under a microscope; however, it is time consuming, and obviously irretrievably damages samples. It is also not suitable for inline/online evaluation [7]. As for nondestructive methods, direct measurement of the thickness with a micrometer is common. In this case, the thickness of the PCB and other materials present without the CC need to be measured beforehand. In addition, it is not possible to obtain the variation in the CC thickness across the sample with a resolution less than millimeters, and perhaps centimeters. It is also rarely possible to measure CC thickness over structures present on the PCB and it should also be understood that micrometer measurement involves contact with the sample surface. Another commonly used method is eddy currents [8]. Although this approach has the potential for high thickness resolution in homogeneous samples, it is difficult to use this to map out the spatial variation of CC thickness on a small scale since the diameter of the probe is usually larger than 5 mm [9]. The approach also only works when the CC is directly over a conductive layer.

Moreover, for current industry standards like IPC-CC-830B [10] and J-STD-001E [11], the thickness measurement for the CC is taken over free and unencumbered surfaces, while important features such as corners and edges of closely spaced conductors are not considered [12]. In addition, it should be also noted that differential wetting of the deposited CC on various proximate materials gives rise to CC thickness differences over those materials; CC thickness measurements on uniform materials will not yield CC thickness and its spatial variation over of complex structures. As we discuss here, terahertz (THz) time-of-flight tomography (TOFT) is a promising nondestructive and noncontact method that can be used for material and structure analysis and for CC thickness measurement and testing [13], [14]. THz TOFT uses short

H. Shi, A. Locquet, and D.S. Citrin are with the School of Electrical and Computer Engineering, Georgia Institute of Technology, Atlanta, Georgia 30332-0250 and Georgia Tech-CNRS IRL2958, Georgia Tech-Europe, 2 Rue Marconi, 57070 Metz, France. Corresponding author: D.S. Citrin, email: david.citrin@ece.gatech.edu. P.J. Singh is with the Materials and Processes Lab, IBM, Poughkeepsie, NY 12601. H. Fu is with International Electronics Manufacturing Initiative, 3000 RDU Center Drive, Suite 220, Morrisville, North Carolina 27560. Maroc Ricci, Serena Calvelli, and Stefano Laureti are with DIMES Department, University of Calabria, Arcavacata (CS), Italy

Manuscript received July 17, 2024; revised MMM DD, 2023.

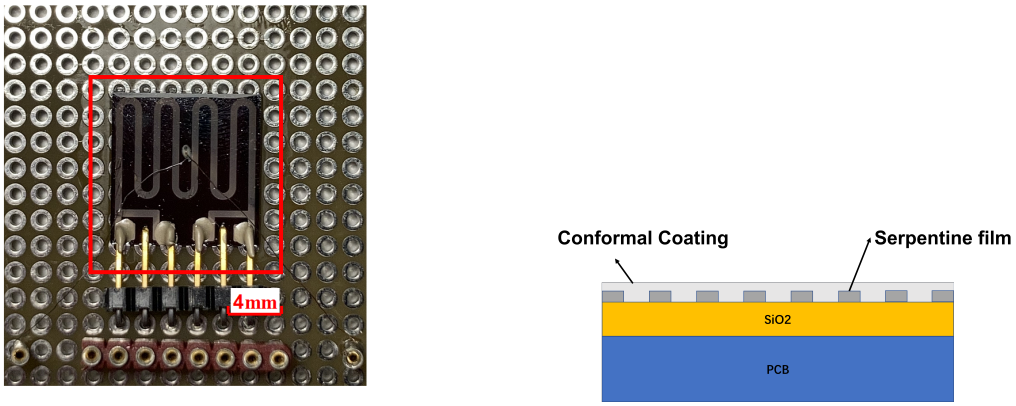

Fig. 1. (a) Photograph of the chip with acrylic CC. The red square area is the region of interest corresponding to the chip. (b) Cross-section of the chip with Ag serpentine film. The substrate is SiO_2.

pulses of THz-frequency electromagnetic radiation to probe the properties of a variety kind of matters. The typical band of ultrafast THz pulses is between 0.1 and 3 THz, corresponding to a wavelength range 30 mm down to 10 µm. It is reported that THz TOFT has the ability to examine delamination in glass fiber-reinforced composite laminates [15] Thickness measurements using THz TOFT for samples such as mill-scale thickness on hot-rolled steel strip [16], [17], silicon wafers [18], dental tissue [19], and automotive paint [20] have been reported [21].

In the present work, we use THz TOFT along with orthogonal matching pursuit (OMP) [22] to measure the CC thickness in a nondestructive and noncontact fashion. A detailed distribution of CC thickness illustrated as line scans (B-scans) and over areas (C-scans) are presented. Also, by applying a Gaussian mixture model (GMM) clustering to the THz signal, we can also locate a region with a high density of defects.

II. Sample and Experiment

Figure 1 presents the structure of the test sample we study. In the top view of the sample in Fig. 1(a), the region of interest studied is indicated by the red square. The entire chip is mounted on a peg PCB. The schematic cross section of the chip is shown in Fig. 1(b), which consists of a serpentine Ag film deposit on SiO_2. A layer of acrylic CC covers the entire chip including the PCB. There is another layer of PCB below SiO_2 which holds the chip. The refractive index for acrylic around 1 THz is assumed to be 1.62 [23].

In this experiment, the THz system was a TPS Spectra 3000 (TeraView Ltd., Cambridge, UK), which is capable of producing a broadband and pulsed THz signal. A schematic diagram of the system is shown in Fig. 2. An ultrafast near-infrared fiber laser triggers quasi-single cycle THz pulses at the photoconductive emitter [24]. The THz pulse band extends from $\sim$ 100 GHz to 3 THz. The emitted THz pulse is incident on the sample near normal incidence (the incidence angle is exaggerated to accommodate the various components of the system in the diagram). The reflected THz signal then impinges on the photoconductive receiver, which is gated by a time-delayed portion of the original near-infrared pulse. In this way, the magnitude and phase of the reflected THz signal is mapped out in time. The study was conducted in a controlled laboratory environment with a temperature of 22 °C and a relative humidity of less than 48 %. The THz signal was directed near normal incidence onto the surface. The sample is scanned with motorized stages in both the X and Y directions with a step size of 100 µm. The sampling period in this experiment is 0.0116 ps. For each data point collected, the length of sample signal is 4096. Before measuring the signal reflected from the sample, a reference signal reflected from bare metal (an essentially perfect reflector) at the same position is measured. The THz pulses employed roughly consist of a single electromagnetic cycle of duration of a few ps covering the band from 0.1 to 3 THz. A detailed description of the THz pulse generation is in Ref. 25.

In the B-scans we plot the raw reflected signal or the reflected signal following analysis–here with GMM. to reveal the location of interfaces that are sufficiently close that their reflections temporally overlap. In this case, the experimental technique is known as THz TOFT. Knowing the refractive indices of the constituent materials, we can translate time delay in the reflected signal to layer thickness to reconstruct the sample' stratigraphy. See Eq. (2) below.

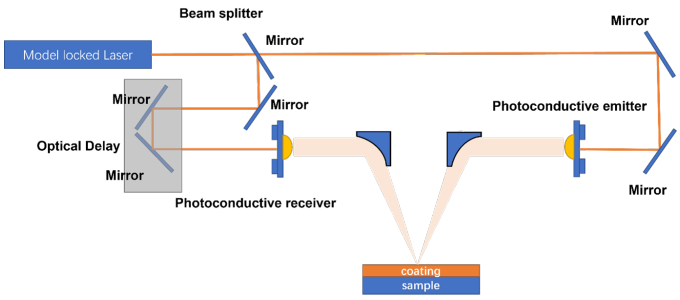

Fig. 2. Schematic diagram of the THz system. An mode-locked ultrafast fiber laser is incident on a fast photoconductor to generate a roughly single-cycle THz pulse covering the band from 0.1 GHz to 3 THz.

III. Methods

A. Gaussian Mixture Model

GMM is a probabilistic model extensively employed in a wide range of applications, including image segmentation [26], anomaly detection [27], and classification [28]. It models the complex data distributions by representing them as a weighted sum of multiple Gaussian components. To implement GMM, we select representative features in the reflected THz signal that are likely to be correlated with the presence and types of defects observed. We then carry out a statistical analysis on the data related to the presence or absence of the selected features to classify the signal as being characteristic or not of a given type of defect. We thus assume that the signal reflected from an area with defects will differs in the distribution of features compared to other areas, *e.g.*, when the diffuse reflection from highly inhomogeneous areas leads to a weaker reflected peak. Specifically, a set of 14 features were selected from the original time-domain signals, which includes the maximum and minimum values, their corresponding temporal positions, median, standard deviation, skew, number of peaks above a certain threshold height (0.05), average width and height of the peaks, kurtosis, and the first, second, and third quantiles. These features effectively represent the measured time-domain signal and facilitate the accurate identification of the reflected signal using GMM clustering.

B. Orthogonal Matching Pursuit

OMP is a deterministic algorithm utilized for sparse data reconstruction. Essentially, the *dictionary* within OMP represents an expansive set of basis functions. Rather than partitioning the data, OMP seeks to express the data in terms of a minimal number of these basis functions. Thus, the objective is to achieve a close approximation of the original data using the fewest dictionary elements possible.

As a greedy algorithm, OMP selects the most important piece at each step and add it to the solution, until the recreated data is close enough to the original data. This method is useful in various fields, such as data compression, signal processing, and image processing. The system can be written as

$$\mu = \mathbf{A}\beta + \mathrm{e} \tag{1}$$

where $\mathbf{A}$ is a 4096×4096 matrix and is called *the dictionary*, each column of which is a delayed version of reference signal. Each column is also known as an atom; μ is the measured reflection signal from chip; β is a vector which represents the impulse response function, the elements of which represent the contribution of the corresponding atom in the dictionary to the measured signal. By iteratively selecting atoms from a dictionary, we can find the atom that has the highest inner product with the residual signal. The new residue will be calculated by subtracting the inner product from residue in the previous iteration.

What we want to reconstruct is the column-vector β which has a sparse form and represents the inner structure of the sample. We also assume that the noise in the measurement is e, which is regarded as Gaussian white noise. By iterating as above, we can obtain the most likely β that reconstruct the system. The iteration will ends when the residue is below a specified error or when a maximum iteration number is reached.

IV. Results and Discussion

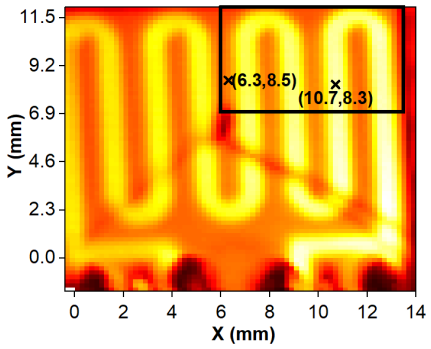

Fig. 3. C-scan of the chip. The contrast mechanism is the peak value of the reflected THz signal.

Figure 3 displays a THz C scan where the contrast mechanism is the peak value of the reflected signal. As metals are excellent THz reflectors, the peak reflected THz field is strongest when the THz pulse is incident over metal as the reflections from the air/CC and CC/SiO_2 interfaces are weaker. As a consequence, the C-scan clearly shows the serpentine metallization.

Figure 4 shows a typical raw A-scan at two points, one on the serpentine film, the other between the metallization. The initial strong peak is the combined reflections from the air/CC and CC/metal or SiO_2 interfaces. Due to the fact that the CC is thin, the two respective echoes from the front and back surfaces of the CC overlap in time and may not be obviously visually distinct. When the incident THz signal is between the serpentine metallization (black), there is a weaker but still clear reflection from the SiO_2/PCB interface, which is not visible when the signal is incident on the metal (red), which as an excellent reflector, shadows underlying features. Also note that because the metal is an excellent reflector, the peak reflection on metal is higher than between the metal.

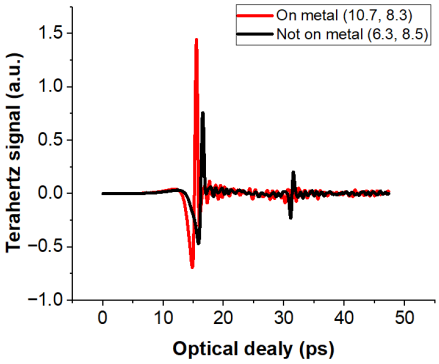

Fig. 4. A-scan at two different points on the sample: (10.7,8.3) is on the serpentine film and (6.3,8.5) is between the serpentine film, both under CC.

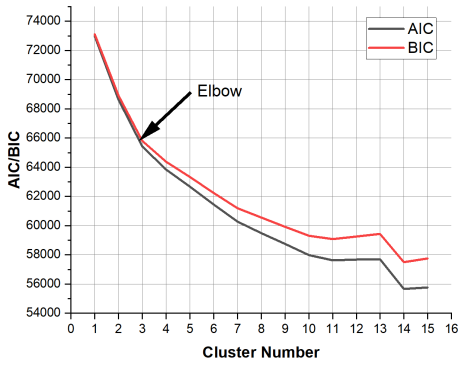

Fig. 5. AIC/BIC with different cluster number.

The feature at 33 ps is a reflection from the back of SiO_2 surface. Note that it is largely absent when the incident pulse is on the metallization as the metal shaddows deeper-lying layers from the incident signal. Although detecting small defects such as individual air bubbles in the CC may be below the resolution of our experiment, single strongly-scattering point defects, larger defects, defect aggregates, and inhomogeneities may be detected even when the individual defects cannot be resolved. The photomicrograph displayed in Fig. 8(a) shows a region where the conformal coating has a high defect density composed of near-surface blisters. (Air bubbles appear to be within the CC under the microscope as various features come into and out of focus as the focus is varied within the CC. Blisters appear on the surface as they are only in focus when the focus is at the air/CC interface.) The grey features in Fig. 8(b) are on the CC surface and may be dust. A region of interest with both types of defects seen in Fig. 4(a) and (b) was selected as the black rectangle in Fig. 3.

In GMM, determining the optimal cluster number is a critical step. To find the suitable number, the Akaike information criterion (AIC) [29] and the Bayesian information criterion (BIC) [30] are widely used and can balance the model complexity with goodness-of-fit. AIC and BIC for different GMM cluster number are shown in Fig. 5. The observation reveals that no apparent global minimum exists for GMM; as the number of clusters increases, both AIC and BIC continue to decrease. Nevertheless, lower AIC and BIC values do not necessarily indicate improved clustering performance in this scenario; instead, the trend suggests the potential for overfitting. Upon examining the plot, it becomes evident that the rate of decrease in both AIC and BIC diminishes beyond three clusters, indicating overfitting. Therefore, the cluster number three is regarded as an elbow point for this particular problem and two or three are potentially suitable numbers to conduct GMM.

The cluster result is shown in Fig. 6. When we set the cluster number as 2, it is obvious that GMM clusters the signal by the criterion if there is serpentine film beneath the point probed or not. When a larger cluster number 3 is employed, except for the similar area as is shown in cluster number 2, there will be a new cluster which is shown as the red area in Fig. 6(b). The new area found is in consistent with an area identified under the microscope as having a high defect density of bubbles.

To extract the CC thickness, OMP is applied. The thickness of the sample can be extracted from

$$d = \frac{c\Delta t}{2n} \tag{2}$$

where Δt is the time delay between the two interfaces which is calculated by the extracted β (*i.e.*, sample number between peaks in β multiplies sampling period), c is the speed of light in free space and n is the refractive index of the CC. It is also assumed that the impulse-response function, which defines the reflected signal, primarily consists of a baseline at zero and a sparse series of sharp peaks connected to reflections from the interfaces. In the impulse-response function, where a reflection is found is assigned "1" while "0" is assigned when reflection is not detected. By doing so, a binary THz B scan can be formed as shown in Fig. 7.

In order to measure the thickness distribution of the CC across the chip, three sections are selected to perform B scans. Intentionally, one line was selected to cross the serpentine structure (y = 9.6 mm), while the other two lines were entirely directly over metal or SiO_2, respectively (x = 9.8 mm, x = 10.8 mm) as shown in Fig. 7. The x-axis in the B scans provides the coordinates of the measure points while the y-axis gives the optical delay at each sample point. In Fig. 7 (b)-(d), the red and orange lines around 15 ps represent the CC/SiO_2 and CC/air interfaces of the CC. For areas without metal, the THz signal was able to penetrate the SiO_2 and reach the bottom SiO_2/PCB interface, which is represented by the green line around 31 ps in the plot. Fig. 7(c) illustrates a B-scan choosing a section without underlying metal whereas Fig. 7(d) represents a B-scan for a section including the serpentine metallization. It is apparent that due to the presence of the metal, the THz signal was more strongly reflected by the CC/metal interface.

The CC thickness can be extracted by Eq. (2). Figure 9(a) shows the thickness distribution of the CC in a section crossing the serpentine metallization. The CC thickness is observed to be nonuniform over the line with a tendency for the thickness to decrease with x. Also striking, the CC thickness over metal is consistently greater than over where the metal is absent. This trend is also evident in the thickness measurements taken along the y direction, as in Fig. 9(b). The average CC thickness along x = 10.8 mm is 64.3 μm while at x = 9.8 mm, the average thickness is 56.2 μm. Furthermore, when looking at the line chosen along the x direction on metal (x = 10.8 mm), we observe a decrease in the thickness starting around y= 9.6mm. [black line in Fig. 9(b)]. However, for the section chosen that is not through the metallization, this kind of behavior is not found [red line in Fig. 9(b)]. This is shown as the grey area in Fig. 9(b). This area is at the apex of the curved section in the serpentine film and the substrate below the CC is gradually changing from metal to SiO_2. Our measurement of sharply varying CC thickness cannot be easily accessed nondestructively by other methods.

A tomograph is generated for the region of interest to better visualize the variation of the CC thickness distribution over the entire chip, as in Fig. 10. The blue surface represents the

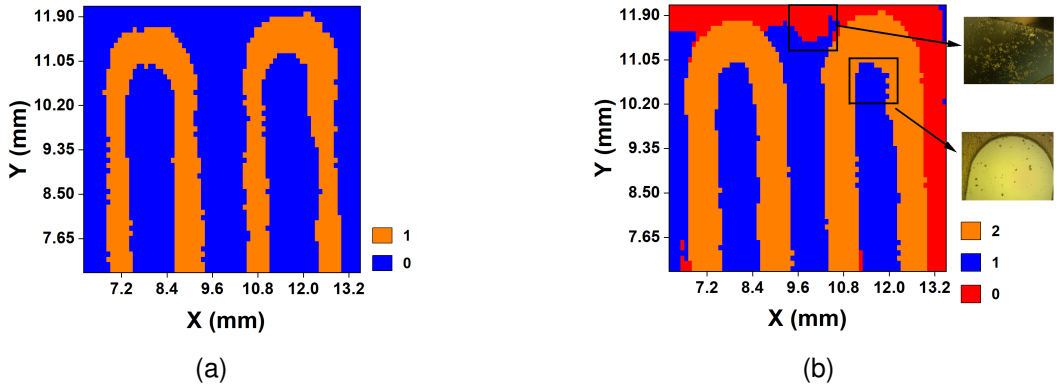

Fig. 6. GMM clustering result for cluster number (a) two and (b) three. The red area in (b) is estimated area with high defect density.

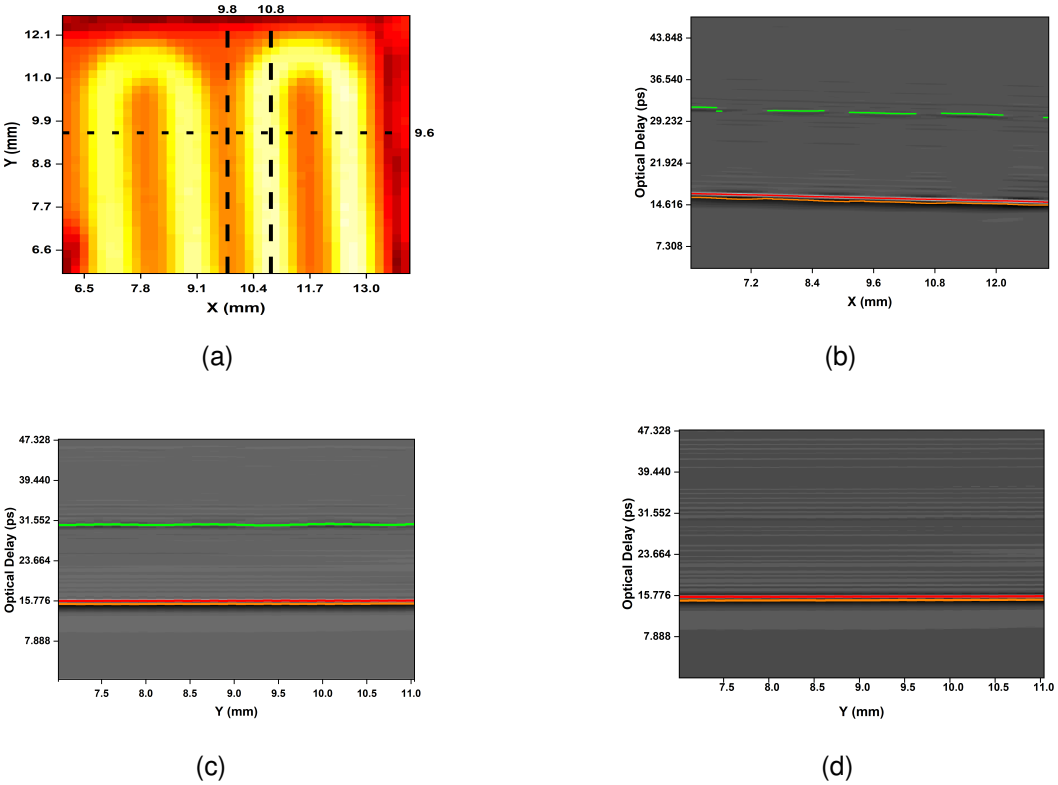

Fig. 7. (a) C-scan where the contrast mechanism is the peak value of the reflected signal and (b)-(d) binary B-scans over lines indicated in the (a) at positions y = 9.6 mm, x = 9.8 mm, and x = 10.8 mm.

CC/ SiO_2 interface while the red surface represents air/CC interface. The thickness distribution over the area is shown in projected onto the XY plane. The total gradual CC thickness variation over the entire sample is $\sim$ 10 μm. The result suggests that the nonuniformity in the CC thickness distribution is primarily due to irregularities on the air/CC interface rather than at the irregular CC/SiO_2 interface. The observation of a thicker CC on metal is consistent with the expectation that the acrylic CC experiences higher cohesive force on Ag than on SiO_2, and thus wets the metal better than the underlying SiO_2. It is also noteworthy that areas that are clustered differently by GMM when the cluster number is 3 also exhibit differences in thickness. Specifically, a decrease in CC thickness is observed near the edge around (x,y) = (10 mm, 11 mm) which may be caused by degradation of the CC as seen in Figs. 8 and 6.

V. Conclusion

We have for the first time demonstrated that THz TOFT combined with OMP and GMM can nondestructively provide CC thickness maps on the sub-mm scale and can identify regions of the CC with high defect density. We find the variation in CC thickness over a serpentine Ag film on the sub-mm scale with thicker CC on the metal than over SiO_2. Thus, THz imaging provides essential information about CCs that is otherwise difficult or currently impossible to access in a nondestructive and noncontact fashion.

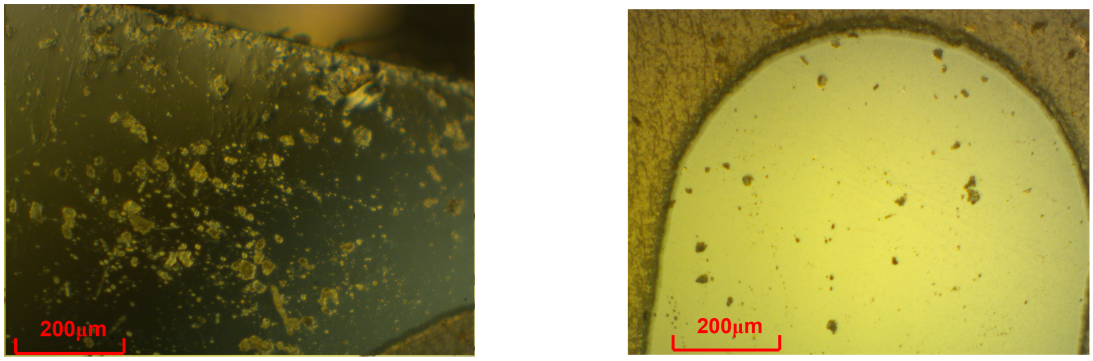

Fig. 8. Photomicrograph of CC with (a) high defect density (bubbles and blisters) and (b) low defect density (surface dust).

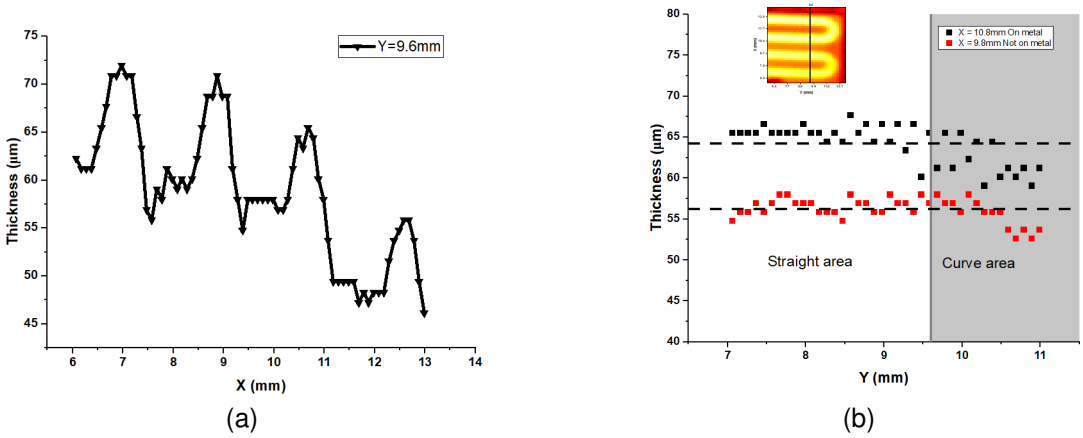

Fig. 9. CC thickness distribution over the three lines in Fig. 6(a): (a) y = 9.6 mm, (b) x =10.8 mm (black), x = 9.8 mm (red). For line x=10.8mm, when y is greater than 9.6 mm, the CC thickness exhibits a decreasing trend.

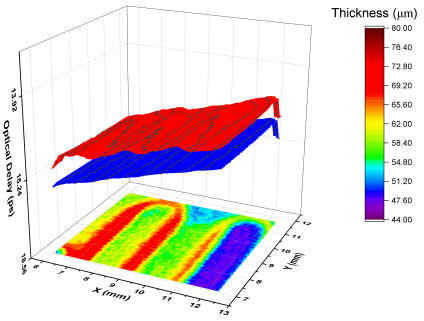

Fig. 10. Tomograph of the layers. The red surface is the air/CC interface while the blue surface is CC/SiO_2 interface. The projection on XY plane is the estimated thickness distribution over the area.

REFERENCES

[1] K. Zhang and M. Pecht, "Effectiveness of ccs on a pbga subjected to unbiased high humidity, high temperature tests," *Microelectronics International*, vol. 17, no. 3, pp. 16–20, 2000.

[2] J. Keeping, "Conformal coatings," in *Lead-free Soldering Process Development and Reliability*, J. Bath, Ed. John Wiley & Sons, 2020, pp. 429–465.

[3] M. Szuch, A. Lewis, H. Pulido, and A. Asymtek, "New coating technologies and advanced techniques in conformal coating," Tech. Rep., 2006.

[4] S. Horn. (2016) 6 conformal coating defects and how to prevent them. Accessed on: 2023-08-25. [Online]. Available: https://blog.paryleneconformalcoating.com/6-conformal-coating-defects-and-how-to-best-avoid-them/

[5] C. Hunt, A. Mensah, A. Buxton, and R. Holman, "Determining conformal coating protection," *Soldering & Surface Mount Technology*, vol. 18, no. 4, pp. 38–47, 2006.

[6] C. Emersic, R. Lowndes, I. Cotton, S. Rowland, and R. Freer, "Degradation of conformal coatings on printed circuit boards due to partial discharge," *IEEE Transactions on Dielectrics and Electrical Insulation*, vol. 23, no. 4, pp. 2232–2240, 2016.

[7] C. Petrilli, "The basics of coating thickness measurement," *Metal Finishing*, vol. 99, no. 8, pp. 8–13, 2001.

[8] X. Liu and H. Lin, "Research on coating thickness measurement with eddy current," in *2018 Eighth International Conference on Instrumentation & Measurement, Computer, Communication and Control (IMCCC)*. IEEE, July 2018, pp. 101–105.

[9] "Measurement of conformal coating on printed circuit boards," 2023, accessed on: 2023-07-09. [Online]. Available: https://www.defelsko.com/resources/measurement-of-conformal-coating-on-printed-circuit-boards

[10] "Qualification and performance of electrical insulating compounds for printed wiring assemblies," Standard IPC-CC-830B, 2008.

[11] "Requirements for soldered electrical and electronic assemblies," Standard IPC J-STD-001E, 2010.

[12] S. Han, M. Osterman, S. Meschter, and M. Pecht, "Evaluation of effectiveness of conformal coatings as tin whisker mitigation," *Journal of Electronic Materials*, vol. 41, pp. 2508–2518, 2012.

[13] M. Naftaly, N. Vieweg, and A. Deninger, "Industrial applications of terahertz sensing: State of play," *Sensors*, vol. 19, no. 19, p. 4203, 2019.

[14] D. S. V. M. L. D. EH, A. Hoffmann, M. Booske, J. Paoloni, C. Gensch, M. Weightman, P. Williams, G. Castro-Camus, and E, "Exploring the

ultimate speed of thz electronics," *Journal of Physics D: Applied Physics*, vol. 50, no. 4, p. 043001, 2017.
[15] J. Dong, B. Kim, A. Locquet, P. Mckeon, N. Declercq, and D. Citrin, "Nondestructive evaluation of forced delamination in glass fiber-reinforced composites by terahertz and ultrasonic waves," *Composites Part B: Engineering*, vol. 79, pp. 667–675, 09 2015.
[16] M. Zhai, A. Locquet, C. Roquelet, J.-L. Borean, P. Meilland, and D. S. Citrin, "Nondestructive tertiary mill-scale thickness measurement on commercial hot-rolled steel strip: Terahertz time-of-flight tomography," *steel research international*, vol. n/a, no. n/a, p. 2300124. [Online]. Available: https://onlinelibrary.wiley.com/doi/abs/10.1002/srin.202300124
[17] M. Zhai, A. Locquet, C. Roquelet, and D. Citrin, "Terahertz time-of-flight tomography beyond the axial resolution limit: Autoregressive spectral estimation based on the modified covariance method," *Journal of Infrared, Millimeter, and Terahertz Waves*, vol. 41, 08 2020.
[18] C. Y. Jen and C. Richter, "Sample thickness measurement with thz-tds: Resolution and implications," *Journal of Infrared, Millimeter, and Terahertz Waves*, vol. 35, pp. 840–859, 2014.
[19] D. Crawley, C. Longbottom, V. P. Wallace, B. Cole, D. Arnone, and M. Pepper, "Three-dimensional terahertz pulse imaging of dental tissue," *Journal of Biomedical Optics*, vol. 8, no. 2, pp. 303–307, 2003.
[20] K. Su, Y. C. Shen, and J. A. Zeitler, "Terahertz sensor for non-contact thickness and quality measurement of automobile paints of varying complexity," *IEEE Transactions on Terahertz Science and Technology*, vol. 4, no. 4, pp. 432–439, 2014.
[21] S. Mukherjee, N. A. Kumar, P. C. Upadhya, and N. Kamaraju, "A review on numerical methods for thickness determination in terahertz time-domain spectroscopy," *The European Physical Journal Special Topics*, vol. 230, no. 23, pp. 4099–4111, 2021.
[22] S. Mallat and Z. Zhang, "Matching pursuits with time-frequency dictionaries," *IEEE Transactions on Signal Processing*, vol. 41, no. 12, pp. 3397–3415, 1993.
[23] M. Zhai, A. Locquet, and D. S. Citrin, "Pulsed thz imaging for thickness characterization of plastic sheets," *NDT & E International*, vol. 116, p. 102338, 2020.
[24] D. H. Auston, "Picosecond optoelectronic switching and gating in silicon," *Applied Physics Letters*, vol. 26, no. 3, pp. 101–103, 09 2008. [Online]. Available: https://doi.org/10.1063/1.88079
[25] J. Dong, A. Locquet, and D. S. Citrin, "Enhanced terahertz imaging of small forced delamination in woven glass fibre-reinforced composites with wavelet de-noising," *Journal of Infrared, Millimeter, and Terahertz Waves*, vol. 37, pp. 289–301, 2016.
[26] H. Bi, H. Tang, G. Yang, H. Shu, and J.-L. Dillenseger, "Accurate image segmentation using Gaussian mixture model with saliency map," *Pattern Analysis and Applications*, vol. 21, no. 3, pp. 869–878, Jul. 2018. [Online]. Available: https://www.hal.inserm.fr/inserm-01674406
[27] B. Zong, Q. Song, M. R. Min, W. Cheng, C. Lumezanu, D. Cho, and H. Chen, "Deep autoencoding gaussian mixture model for unsupervised anomaly detection," in *International Conference on Learning Representations*, 2018. [Online]. Available: https://openreview.net/forum?id=BJJLHbb0-
[28] J. Zhang, X. Hong, S.-U. Guan, X. Zhao, H. Xin, and N. Xue, "Maximum gaussian mixture model for classification," in *2016 8th International Conference on Information Technology in Medicine and Education (ITME)*, 2016, pp. 587–591.
[29] H. Akaike, "A new look at the statistical model identification," *IEEE Transactions on Automatic Control*, vol. 19, no. 6, pp. 716–723, 1974.
[30] G. Schwarz, "Estimating the Dimension of a Model," *The Annals of Statistics*, vol. 6, no. 2, pp. 461 – 464, 1978. [Online]. Available: https://doi.org/10.1214/aos/1176344136

VI. Biography Section

Haolian Shi Received the B.S. degree in Physics from China University of Mining and Technology, Jiangsu Province, China. He is currently working toward the Ph.D. degree in Electrical and Computer Engineering at the Georgia Institute of Technology.

His research interests include terahertz imaging and spectroscopy, nondestructive testing, material characterization, and machine learning.

Min Zhai received the M.S. degree in Microelectronics and Solid State Electronics from Wuhan University, Hubei Province, China, and Ph.D. degree in electrical and computer engineering at the Georgia Institute of Technology Atlanta, GA, USA.

His research interests include terahertz imaging and spectroscopy, nondestructive evaluation, material characterization, and birefringence.

Alexandre Locquet received the M.S. degree in Electrical Engineering from the Faculté Polytechnique de Mons, Mons, Belgium, the Ph.D. degree (doctorat) in Engineering Science and Electrical and Computer Engineering from the Université de Franche-Comté, Besanson, France, and the Ph.D. degree in Electrical and Computer Engineering from the Georgia Institute of Technology (Georgia Tech), Atlanta, GA, USA.

He is currently a Researcher with the International Research Laboratory, Georgia Tech-CNRS IRL2958 at Georgia Tech Europe in Metz, France, and an Adjunct Professor with the School of Electrical and Computer Engineering, Georgia Tech. His research interests include semiconductor laser dynamics and chaos, nonlinear time-series analysis, physical-layer security, and terahertz imaging.

Dr. Locquet is a member of Eta Kappa Nu, the Optical Society of America, and the IEEE Photonics Society.

D.S. Citrin (M'93-SM'03) received the B.A. degree in Physics from Williams College, Williamstown, MA in 1985 and the M.S. and Ph.D. degrees in Physics from the University of Illinois, Urbana, IL in 1987 and 1991, respectively. From 1992 to 1993, he was a Postdoctoral Research Fellow with the Max Planck Institute für Festkörperforschung, Stuttgart, Germany, where he conducted research on exciton radiative decay in low-dimensional semiconductor structures. Subsequently, from 1993 to 1995, he was a Center Fellow with the Center for Ultrafast Optical Science, University of Michigan, Ann Arbor, MI where he researched ultrafast phenomena in quantum wells. He was then an Assistant Professor of Physics with Washington State University, Pullman, WA, from 1995 to 2001. In 2001, he joined the faculty of the Georgia Institute of Technology, Atlanta, GA, where he is currently a Professor of Electrical and Computer Engineering. In addition, he coördinates the research effort on nondestructive evaluation with the international research laboratory Georgia Tech-CNRS IRL2958, Georgia Tech-Europe, Metz, France. His research interests include terahertz science and technology, heterogeneous packaging, microwave photonics, quasiperiodic lattices, nonlinear dynamics of external-cavity semiconductor lasers, nanophotonics, and archæometry.

Citrin is a former Associate Editor of the IEEE JOURNAL OF QUANTUM ELECTRONICS. He was a recipient of a Presidential Early Career Award for Scientists and Engineers (PECASE), an award under the US Office of Naval Research Young Investigator Program (YIP), and of a Friedrich Bessel Prize from the Alexander von Humboldt Stiftung.